Determining the carrier-envelope phase of relativistic laser pulses via electron-momentum distribution

Yan-Fei Li,[1] Jian-Xing Li,[1,*] Karen Z. Hatsagortsyan,[2,†] Yong-Tao Zhao,[1,‡] Bo Zhang,[3,4] Yu-Tong Li,[5,6] Yang-Yang Liu,[1] Ze-Long Zhang,[1] Zhong-Feng Xu,[1] and Christoph H. Keitel[2]

[1]*School of Science, Xi'an Jiaotong University, Xi'an 710049, China*

[2]*Max-Planck-Institut für Kernphysik, Saupfercheckweg 1, 69117 Heidelberg, Germany*

[3]*Department of High Energy Density Physics, Research Center of Laser Fusion, Mianyang 621900, Sichuan, China*

[4]*Science and Technology on Plasma Physics Laboratory, Research Center of Laser Fusion, Mianyang 621900, Sichuan, China*

[5]*Beijing National Laboratory for Condensed Matter Physics, Institute of Physics, Chinese Academy of Sciences, Beijing 100190, China*

[6]*School of Physical Sciences, University of Chinese Academy of Sciences, Beijing 100049, China*

(Received 6 September 2018; published 29 January 2019)

The impact of the carrier-envelope phase (CEP) of a long relativistic tightly focused laser pulse on the dynamics of a counterpropagating electron beam has been investigated theoretically in the, so-called, electron reflection regime. Our semiclassical Monte Carlo simulations show that the electrons are reflected at the rising edge of the laser pulse due to the ponderomotive force of the focused laser beam, and an asymmetric electron-momentum distribution emerges along the laser polarization direction, which sensitively depends on the CEP of the driving laser pulse for weak radiative stochasticity effects. The CEP signatures can be determined in the electron-momentum distribution at laser intensities of the order or larger than $10^{19}\,\mathrm{W/cm^2}$ and for the pulse lengths up to 10 cycles. The CEP detection resolution is proportional to the electron beam density and can achieve approximately 0.1° at an electron density of about $10^{15}\ \mathrm{cm^{-3}}$. The method is applicable for currently available ultraintense laser facilities with the laser peak power ranging from tens of terawatt to multipetawatt.

DOI: 10.1103/PhysRevA.99.013850

I. INTRODUCTION

In the past decade remarkable progress has been achieved in laser technique pushing the limits of the chirped pulse amplification method [1]. With short laser pulses a large peak power is reached at relatively low pulse energies, allowing development of terawatt lasers and large scale petawatt facilities, and paving a way for relativistic laser pulses, nowadays available up to a peak intensity of $10^{22}\,\mathrm{W/cm^2}$ [2–5]. Intense lasers have many applications, e.g., for laser electron or ion acceleration [6–8], x- or γ-ray radiation sources [9–12], inertial confinement fusion [13–15], and for laboratory astrophysics [16–18].

The carrier-envelope phase (CEP) of a laser pulse, i.e., the phase of the carrier wave with respect to the intensity envelope of the pulse, is a crucial parameter to characterize the waveform of the field and usually varies due to the difference between phase and group velocity in a train of multiple pulses. In a short laser pulse the field asymmetry is CEP dependent and significantly affects the laser-matter interaction. In particular, the asymmetry between positive and negative values of the laser field (or of the vector-potential) yields in the nonrelativistic regime several effects in strong field ionization, such as asymmetry in the ion momentum distribution in nonsequential double ionization [19] and electron localization during molecular photodissociation [20], controls the quantum interference [21], influences electron quantum paths contributing to harmonic generation [22], and allows for isolated attosecond pulses in high-order harmonic generation [23,24]. The same field asymmetry in the relativistic regime can modify the radiation spectra in nonlinear Compton scattering [25–27], the momentum distribution [28–31], and the differential cross sections of the Breit-Wheeler pair production process [32], as well as the interferences between different pair production channels [33]. In particular, the angular distribution of the electron radiation [26], has been proposed for CEP detection of relativistic ultrashort laser pulses with the pulse duration less than two cycles.

However, as already was pointed out in Ref. [34], the CEP effect can have a different character in the nonrelativistic and relativistic regimes. While in the nonrelativistic regime the CEP effect mostly depends on the asymmetry of the field around the laser pulse peak, in the relativistic regime some CEP effects are due to field asymmetry in the rising edge of the laser pulse, which can be conspicuous even in multicycle pulses and provide a way for CEP measurement for the common multicycle (up to 10 cycles and above 33 fs) relativistically intense laser beams [2–8,35–39]. Separating a fraction of such beam and applying conventional nonrelativistic methods for CEP measurement, such as the stereographic above-threshold ionization (ATI) [40], the f-$2f$ interferometry [41], the direct phase measurement method based on multi-photon-induced photoelectron emission [42], and the streaking methods [43], is not possible in this case, as these methods are designed for few-cycle pulses. However, the

*jianxing@xjtu.edu.cn
†k.hatsagortsyan@mpi-hd.mpg.de
‡zhaoyongtao@xjtu.edu.cn

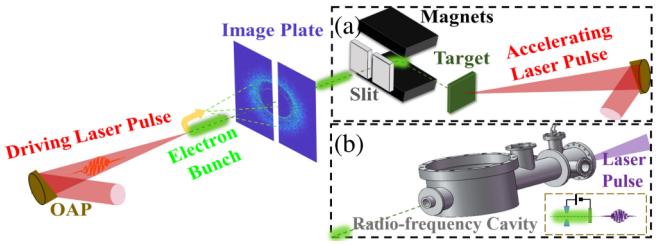

FIG. 1. The conceptual scenario of the CEP detection via the electron-momentum distribution. The driving laser pulse is focused by an off-axis paraboloid (OAP) and collides head-on with an electron bunch in the $\gamma \ll \xi/2$ regime. The bunch is produced either by (a) laser-plasma accelerator (a laser pulse ionizes the low-density target and accelerates the electrons forwards; the magnets and the slit select electron energy), or (b) radio-frequency (RF) electron gun (a laser pulse illuminates a photocathode in the RF cavity, and the emitted electrons are accelerated to a relativistic energy by the cavity RF field). Due to the laser focusing effect, the electrons are reflected by the rising edge of the driving laser and move backwards. The CEP of the driving laser pulse is extracted from the asymmetric transverse momentum distribution of electrons on the image plate.

CEP detection of multicycle 20-fs pulses in the nonrelativistic regime via the spectral characteristics of high-order harmonic radiation is feasible and has been demonstrated in Ref. [22]. An example of the CEP determination of long relativistic laser pulses has been demonstrated in Ref. [34] by employing the fine features of the electron radiation x-ray spectra. The method, however, is applicable only for extreme laser intensities $I_0 \gtrsim 10^{22}\,\mathrm{W/cm^{-2}}$, keeping open the problem of the CEP measurement of laser pulses in an intensity range from 10^{19} to $10^{22}\,\mathrm{W/cm^2}$, mostly produced in current ultraintense laser facilities.

In this paper, we investigate theoretically the CEP determination of relativistic multicycle laser pulses with peak intensities $I_0 \gtrsim 10^{19}\,\mathrm{W/cm^2}$, exploiting the momentum distribution of the electron beam after the interaction. The relativistic laser pulse interacts with a counterpropagating electron beam. The electron energy is considered to be much smaller than the reflection condition [44], i.e., $\gamma \ll \xi/2$, with the electron Lorentz factor γ, and the dimensionless parameter of the laser field $\xi \equiv eE_0/(m\omega_0)$. Here, E_0 and ω_0 are the amplitude and frequency of the laser field, respectively, and $-e$ and m the electron charge and mass, respectively. Planck units $\hbar = c = 1$ are used throughout. Due to the laser focusing effect, the electrons are reflected by the rising edge of the driving laser pulse and move backwards, see the interaction scenario in Fig. 1. The electron beam can be generated by either the laser-plasma accelerators [7,45], or the radio-frequency (RF) electron gun system [46–48]. We choose conditions when the stochasticity effects in the electron radiation are weak [49–51], i.e., the invariant quantum parameter $\chi \equiv |e|\sqrt{(F_{\mu\nu}p^\nu)^2}/m^3 \ll 1$ [52,53], where $F_{\mu\nu}$ is the field tensor, and $p^\nu = (\varepsilon, \mathbf{p})$ the incoming electron 4-momentum. In this case the electron final transverse momentum distribution is asymmetric. The asymmetry sensitively depends on the CEP of the driving laser pulse and can be employed for CEP determination. This method does not rely on the electron radiation and, therefore, is applicable at much lower laser intensities ($\xi \gtrsim 5$) than the CEP determination via the x-ray spectra ($\xi \gtrsim 100$) [34]. Meanwhile, the resolution of the CEP determination in this method is much higher than that in [34], since the diffraction limitation of an electron is much smaller than that of a photon. The asymmetry due to CEP is larger in the rising edge of the laser pulse than near the peak, which allows the application of the method for rather long laser pulses ($\lesssim$10 cycles, $\sim 30-40\,fs$) and even for longer flat-top laser pulses ($\lesssim$20 cycles).

This paper is organized as follows. In Sec. II we discuss the applied theoretical method for the calculation of the electron dynamics and radiation. We calculate and analyze the CEP-dependent electron-momentum distribution in Sec. III. In Sec. IV we investigate the impacts of the laser and electron beam paramters on the CEP determination. And, a brief conclusion of this work is represented in Sec. V.

II. APPLIED THEORETICAL METHOD

In relativistic regime, as considered $I_0 \gtrsim 10^{19}\,\mathrm{W/cm^2}$ ($\xi \gtrsim 5$), the quantum radiation-reaction effects could still not be negligible, since $\chi \sim 10^{-6}\xi\gamma$. To keep the consistency of the simulations, we carry out the calculation of the radiation based on Monte Carlo approaches employing QED theory for the electron radiation and classical equations of motion for the propagation of electrons between photon emissions [54–56]. The photon emission probability in the local constant field approximation is used.

In superstrong laser fields $\xi \gg 1$, the photon emission probability W is determined by the local electron trajectory, consequently, by the local value of the parameter χ [53]:

$$\frac{d^2W_{fi}}{d\tilde{\eta}dr_0} = \frac{\sqrt{3}\alpha\chi\left[\int_{r_\chi}^{\infty} K_{5/3}(x)dx + 9r_0r_\chi\chi^2K_{2/3}(r_\chi)/4\right]}{2\pi\lambda\!\!\!^{-}_c(k\cdot p_i)},$$

where $r_0 = \frac{2(k\cdot k')}{3\chi(k\cdot p_i)}$, $\tilde{\eta} = (k\cdot\tilde{r})$, and k, k', $\tilde{r}$, and p_i are the four-vector of the wave vector of the driving laser, the wave vector of the radiated photon, the coordinate, and the momentum of the electron before the radiation, respectively. The Compton wavelength $\lambda\!\!\!^{-}_c = 1/m$ and $r_\chi = r_0/(1-3\chi r_0/2)$. The photon emission of electrons is considered to be a Monte Carlo stochastic process [54–56]. During the electron-laser interaction, for each propagation coherent length $\Delta\tilde{\eta}$, the photon emission will take place if the condition $(dW_{fi}/d\tilde{\eta})\Delta\tilde{\eta} \geqslant N_r$ is fulfilled, where N_r is a uniformly distributed random number in [0, 1]. Herein, the coherent length $\Delta\tilde{\eta}$ is inversely proportional to the invariant laser field parameter ξ; i.e., $\Delta\tilde{\eta} \sim 1/\xi$. However, to keep the total photon emission energy consistent, i.e., to exclude numerical error of the simulation of photon emission, we choose $\Delta\tilde{\eta} \ll 1/\xi$. The photon emission probability

$$W_{fi} = \Delta\tilde{\eta}\frac{dW_{fi}}{d\tilde{\eta}} = \Delta\tilde{\eta}\int_{\omega_{\min}}^{\omega_{\max}}\frac{d^2W_{fi}}{d\tilde{\eta}d\omega}d\omega,$$

where $\omega_{\min}$ and $\omega_{\max}$ are assumed to equal the driving laser photon energy and the electron instantaneously kinetic energy, respectively. In addition, the emitted photon frequency ω_R is

determined by the relation

$$\frac{1}{W_{fi}}\int_{\omega_{\min}}^{\omega_R}\frac{dW_{fi}(\omega)}{d\omega}d\omega=\frac{\Delta\tilde{\eta}}{W_{fi}}\int_{\omega_{\min}}^{\omega_R}\frac{d^2W_{fi}(\omega)}{d\tilde{\eta}d\omega}d\omega=\tilde{N}_r,$$

where, $\tilde{N}_r$ is another independent uniformly distributed random number in [0, 1]. Between the photon emissions, the electron dynamics in the laser field is governed by classical equations of motion:

$$\frac{d\mathbf{p}}{dt}=e(\mathbf{E}+\mathbf{v}\times\mathbf{B}),$$

where $\mathbf{p}$ and $\mathbf{v}$ are the electron momentum and velocity, respectively, and $\mathbf{E}$ and $\mathbf{B}$ are the electric and magnetic fields of the laser pulse, respectively. Given the smallness of the emission angle $\sim 1/\gamma$ for an ultrarelativistic electron, the photon emission is assumed to be along the electron velocity. The photon emission induces the electron-momentum change $\mathbf{p}_f \approx (1-\omega_R/|\mathbf{p}_i|)\mathbf{p}_i$, where $\mathbf{p}_{i,f}$ are the electron momentum before and after the emission, respectively.

At some applicable parameters with rather small χ, the electron dynamics can be also described by Landau-Lifshitz equation [57,58], or even by Newton equation at $\chi \lesssim 10^{-3}$, giving similar results; see the details in the Appendix.

We consider a linearly polarized and tightly focused laser pulse with a Gaussian temporal profile propagating along $+z$ direction and polarized in x direction. The spatial distribution of the fields takes into account up to the ϵ^3 order of the nonparaxial corrections, and the expressions of the electromagnetic fields are presented in the following [59,60]:

$$\begin{aligned}
E_x &= -iE\left[1+\epsilon^2\left(f^2\widetilde{x}^2-\frac{f^3\rho^4}{4}\right)\right],\\
E_y &= -iE\epsilon^2 f^2\widetilde{x}\widetilde{y},\\
E_z &= E\left[\epsilon f\widetilde{x}+\epsilon^3\widetilde{x}\left(-\frac{f^2}{2}+f^3\rho^2-\frac{f^4\rho^4}{4}\right)\right],\\
B_x &= 0,\\
B_y &= -iE\left[1+\epsilon^2\left(\frac{f^2\rho^2}{2}-\frac{f^3\rho^4}{4}\right)\right],\\
B_z &= E\left[\epsilon f\widetilde{y}+\epsilon^3\widetilde{y}\left(\frac{f^2}{2}+\frac{f^3\rho^2}{2}-\frac{f^4\rho^4}{4}\right)\right],
\end{aligned}$$

where,

$$E=E_0F_n f e^{-f\rho^2}e^{i(\eta+\psi_{\rm CEP})}e^{-\frac{t^2}{\tau^2}},$$

E_0 is the amplitude of the laser fields with normalization factor $F_n = i$ to keep $\sqrt{E_x^2+E_y^2+E_z^2}=E_0$ at the focus, yielding the scaled coordinates

$$\widetilde{x}=\frac{x}{w_0},\quad \widetilde{y}=\frac{y}{w_0},\quad \widetilde{z}=\frac{z}{z_r},\quad \rho^2=\widetilde{x}^2+\widetilde{y}^2,$$

where $\epsilon = w_0/z_r$, $z_r=\frac{k_0w_0^2}{2}$ is the Rayleigh length, $f=\frac{i}{\widetilde{z}+i}$, $\eta=\omega_0 t-k_0 z$, τ is the laser pulse duration, $\psi_{\rm CEP}$ is the carrier-envelope phase, the laser wave vector $k_0=2\pi/\lambda_0$, and, λ_0, w_0, and ω_0 are the wave length, focal radius, and the frequency of the laser pulse, respectively.

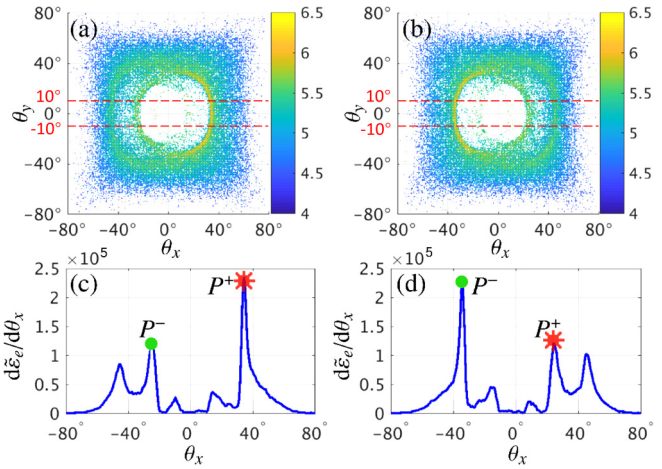

FIG. 2. (a), (b) Angle-resolved electron energy $\log_{10}[d^2\varepsilon_e/(d\theta_x d\theta_y)]$ rad^{-2} in units of m vs. the transverse deflection angles of the electron momenta $\theta_x = \arctan(p_x/p_z)$ and $\theta_y = \arctan(p_y/p_z)$ with the CEP $\psi_{\rm CEP}=0^\circ$ and 180°, respectively. (c), (d) $d\tilde{\varepsilon}_e/d\theta_x$ vs. θ_x with $\psi_{\rm CEP}=0^\circ$ and 180°, respectively. Here, $d\tilde{\varepsilon}_e/d\theta_x = \int_{-10^\circ}^{10^\circ} d^2\varepsilon_e/[d\theta_x d\theta_y]\, d\theta_y$: the total angle-resolved electron energy in the angle region of $-10^\circ \leqslant \theta_y \leqslant 10^\circ$ [shown by red-dashed horizontal lines in (a) and (b)]. And, the peaks in the regions of $\theta_x < 0^\circ$ and $\theta_x > 0^\circ$ are marked by the green-circle P^- and the red-star P^+, respectively. The employed laser and electron parameters are given in the text.

III. RESULTS AND ANALYSIS

A typical example of the angle-resolved electron-momentum distribution in the considered regime, which will be employed further for the CEP determination, is numerically simulated and presented in Fig. 2. The peak intensity of the laser pulse is $I_0 \approx 5\times 10^{20}\,\mathrm{W/cm^2}$ ($\xi=20$), $\lambda_0=1\ \mu$m, $\tau=6T_0$, T_0 is the laser period, and $w_0=2\,\mu$m. An electron bunch of a cylindrical form collides head-on with the laser pulse at the polar angle $\theta_e=179^\circ$ and the azimuthal angle $\phi_e=0^\circ$. The electron mean initial kinetic energy is $\varepsilon_i=0.1$ MeV ($\gamma\approx 0.2$, and $\chi_{\max}\approx 3\times 10^{-5}$), the electron bunch radius $w_e=2\lambda_0$, the length $L_e=6\lambda_0$, and the density $n_e\approx 10^{15}$ cm^{-3}. The energy and angular spreads are $\Delta\varepsilon_i/\varepsilon_i=0.05$ and $\Delta\theta=0.02$, respectively. The electrons in the bunch have a Gaussian distribution in the transverse direction and a uniform distribution in the longitudinal one.

Since $\gamma \ll \xi/2$, the electrons are reflected and move backwards due to the the ponderomotive force caused by the laser focusing (the condition of $w_0 \approx w_e \sim \lambda_0$ is required to ensure the laser focusing effects are important). During the reflection process, the electron dynamics is sensitively governed by the laser field, and, consequently, the field structural information, in particular CEP, is encoded in the final electron-momentum distribution; see Fig. 2. For the cases of $\psi_{\rm CEP}=0^\circ$ and 180°, the electron energy distribution is almost symmetric, and the slight deviation from the symmetry stems from the head-on colliding angle of the electron bunch $\theta_e=179^\circ$ (not exact 180° for the experimental feasibility). For inspecting the main asymmetry features, i.e., the asymmetric electron-momentum distribution along the polarization direction or with respect to θ_x, the electron distributions in Figs. 2(a) and 2(b) are

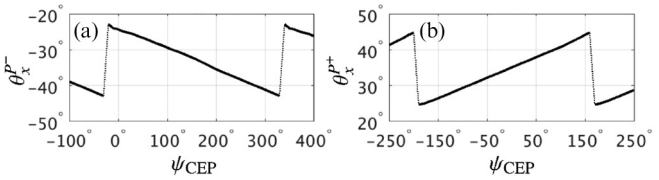

FIG. 3. (a), (b) The variations of $\theta_x^{P^-}$ and $\theta_x^{P^+}$ corresponding to θ_x of P^- and P^+ with respect to ψ_{CEP}, respectively. The laser and electron parameters are the same as in Fig. 2.

integrated over θ_y from -10° to 10°, see Figs. 2(c) and 2(d), respectively [the integration region is indicated by the horizontal lines in Figs. 2(a) and 2(b)]. The deflection angle of the electron momenta $\theta_x = \arctan(p_x/p_z)$ with respect to the laser polarization direction is strongly CEP-dependent. In the regions of $\theta_x < 0^\circ$ and $\theta_x > 0^\circ$, the angle-resolved electron energy distribution $d\tilde{\varepsilon}_e/d\theta_x$ has two peaks indicated by P^- (green circle) and P^+ (red star). The angles θ_x corresponding to P^- and P^+ are denoted by $\theta_x^{P^-}$ and $\theta_x^{P^+}$, respectively.

As the CEP varies within one period, $\theta_x^{P^-}$ ($\theta_x^{P^+}$) monotonously decreases (increases) approximately by 20.05° (20.05°), namely, from -22.92° to -42.97° (from 24.64° to 44.69°); see Figs. 3(a) and 3(b). Taking into account that an angular resolution less than 0.1 mrad is achievable with current technique of electron detectors [61–64], we may conclude that the CEP resolution here could reach $\sim 0.1^\circ$. Since the resolution of the electron detector is proportional to the electron density, therefore, a higher CEP resolution is feasible with a higher density electron bunch.

We also investigate the case with an energy spread of 0.1, and other parameters are the same as those described in the caption of Fig. 2, as shown in Fig. 4. The simulation results keep consistent.

The CEP signatures on electron dynamics are analyzed in Fig. 5. First, the E_z components of the focused laser fields with $\psi_{CEP} = 0^\circ$ and 180° at the point of $(0.5\lambda_0, 0, 0)$ are compared in Fig. 5(a). Note that $E_z = 0$ in a plane wave. The corresponding dynamics of the longitudinal momentum p_z of a sample electron propagating in those laser fields are illustrated in Figs. 5(b) and 5(c). For intuitive understanding let us neglect for a moment radiation reaction, which in fact has a minor contribution in the considered regime. In this case the plane wave laser field could not modify the electron dynamics after the laser-electron interaction [59] [see

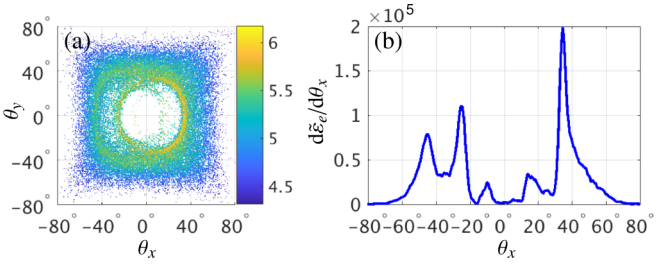

FIG. 4. (a) Angle-resolved electron energy $\log_{10}[d^2\varepsilon_e/(d\theta_x d\theta_y)]$ rad^{-2} vs. θ_x and θ_y, and (b) $d\tilde{\varepsilon}_e/d\theta_x$ vs. θ_x with $\psi_{CEP} = 0^\circ$, with an energy spread of 0.1. Other parameters are the same as those described in the caption of Fig. 2.

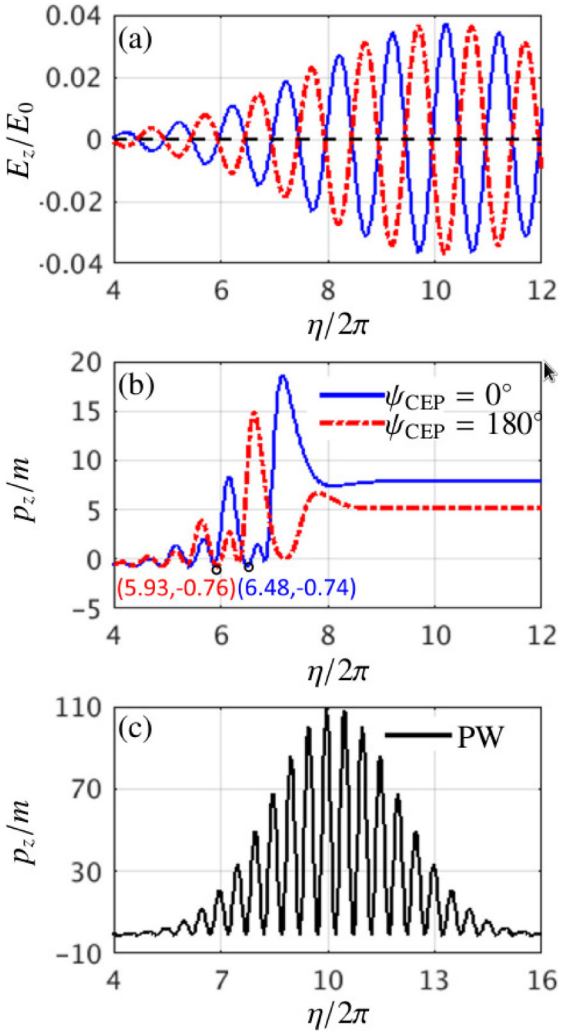

FIG. 5. (a) The longitudinal component of electric field E_z of the focused laser beam (scaled by the laser field amplitude E_0) vs. the laser phase η, at the position $(0.5\lambda_0, 0, 0)$: (blue-solid) $\psi_{CEP} = 0^\circ$ and (red-dash-dotted) $\psi_{CEP} = 180^\circ$. The longitudinal momentum p_z of a sample electron: (b) in the focused laser field with $\psi_{CEP} = 0^\circ$ (blue-solid), and $\psi_{CEP} = 180^\circ$ (red-dash-dotted); (c) in the plane wave (PW) with a six-cycle Gaussian envelope. In (b), the coordinates (5.93, −0.76) (red) and (6.48, −0.74) (blue) indicate the lowest values of p_z oscillations in red and blue curves, respectively. Other laser and electron parameters are the same as in Fig. 2.

Fig. 5(c)], because the electron cannot absorb laser photons from a plane wave field due to the momentum conservation. However, in the focused laser field the electron can absorb laser photons due to an additional ponderomotive momentum transfer to the field which stems from the transverse gradient of the laser field and, therefore, the laser focusing effect induces the electron reflection. Since $\gamma \ll \xi/2$ for the applied parameters, the electrons are reflected at the rising edge of the laser pulse [at $\eta/2\pi \approx 7$, see Fig. 5(b)], and with different CEPs the electron dynamics is apparently different.

Furthermore, we follow the tracks of a group of sample electrons near the laser polarization plane ($y = 0$). The initial coordinate distribution of the sample electrons are given in Fig. 6(a). The electrons initially distributed along the

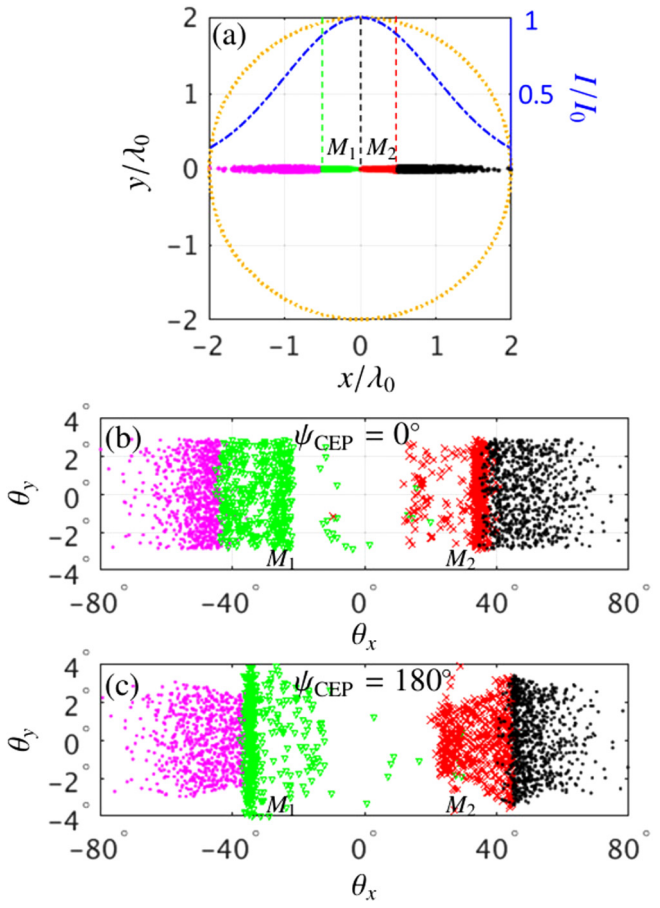

FIG. 6. (a) The initial transverse coordinate distribution of the sample electrons near the laser polarization plane ($y = 0$), and the yellow circle shows the boundary of the electron bunch. The blue-dash-dotted curve represents the transverse Gaussian profile of the laser intensity I scaled by the peak intensity I_0. The sample electrons from left to right are marked in purple, green (M_1), red (M_2), and black. Panels (b) and (c) display the final transverse momentum distributions of the sample electrons of (a) in the focused laser fields with $\psi_{CEP} = 0°$ and 180°, respectively. The same color represents the same group of sample electrons, the left and right sample electrons are marked in circle, and the sample electrons in the regions of M_1 and M_2 are marked in triangle and cross, respectively. Other laser and electron parameters are the same as in Fig. 2.

transverse profile of the laser field [e.g., marked in purple, green (M_1), red (M_2), and black from left to right] are subjected to different transversal gradient of the laser field dI/dx,

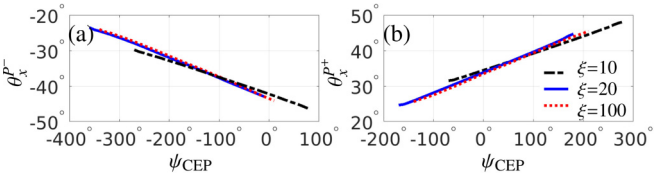

FIG. 7. (a), (b) The variations of $\theta_x^{P^-}$ and $\theta_x^{P^+}$ with respect to the CEP, respectively. The black-dash-dotted, blue-solid, and red-dotted curves represent the cases of $\xi = 10$, 20, and 100, respectively, and the corresponding electron energies $\varepsilon_i = 45$ keV, 100 keV, and 2 MeV, respectively. Other parameters are the same as in Fig. 2.

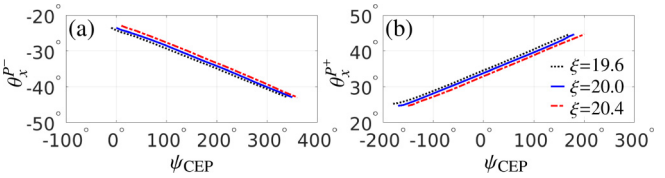

FIG. 8. (a), (b) The variations of $\theta_x^{P^-}$ and $\theta_x^{P^+}$ with respect to the CEP when $\xi = 19.6$, 20, and 20.4, respectively. Other parameters are the same as those described in the caption of Fig. 2.

which determines the final angular spread; see Figs. 6(b) and 6(c). For the electrons initially near the intensity peak [the bands marked in green-triangle (M_1) and red-cross (M_2)], the intensity transverse gradient is rather small and, therefore, the final angular spread is small. Consequently, electron density peaks are formed mostly by those electrons initially near the beam center. Moreover, the dynamics of electrons in different bands are CEP-dependent, cf. Figs. 6(b) with 6(c), which are exhibited in the CEP governed final angular asymmetry.

IV. THE IMPACTS OF THE LASER AND ELECTRON BEAM PARAMETERS ON THE CEP DETERMINATION

We further investigate the impact of the laser and electron parameters on the CEP determination. The dependence on the laser intensity is illustrated in Fig. 7. For $\xi = 10$, 20, and 100, $\Delta\theta_x^{P^-} = \text{Max}(\theta_x^{P^-})\text{-Min}(\theta_x^{P^-}) = 16.65°$, 20.05°, and 20.08°, respectively, and $\Delta\theta_x^{P^+} = 16.62°$, 20.05°, and 19.93°, respectively. The gradient increases with ξ in the region of $\xi \lesssim 20$ and becomes stable as $\xi \gtrsim 20$. The CEP resolutions are approximately 0.12°, 0.1°, and 0.1°, respectively. Thus, the CEP resolution decreases with higher ξ parameter in the domain of $\xi \lesssim 20$. As ξ decreases, the required ε_i decreases as well to satisfy the condition $\gamma \ll \xi/2$. However, ξ is limited from below by the requirement of the relativistic interaction, which is a prerequisite for the applied regime.

For realistic experimental conditions, the petawatt laser pulse energy can be detected with an uncertainty of about 1.5% [65] (usually better than 1% for the-state-of-the-art terawatt laser pulses [66]). We find that an uncertainty of 4% (1%) in the laser energy brings an uncertainty in the CEP detection of about 2.8% (1.1%), see Figs. 8 and 9, which is better than recent experimental achievement for few-cycle multiterawatt laser systems [66].

The dependence of the proposed CEP signature on the laser pulse duration is analyzed in Fig. 10. We compare the variations of $\theta_x^{P^-}$ and $\theta_x^{P^+}$ with respect to the CEP for Gaussian

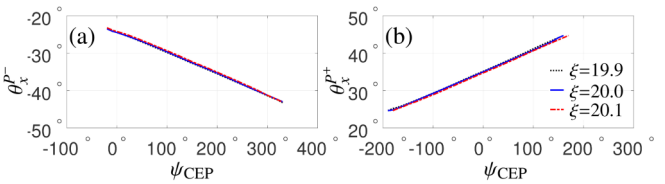

FIG. 9. (a), (b) The variations of $\theta_x^{P^-}$ and $\theta_x^{P^+}$ with respect to the CEP when $\xi = 19.9$, 20, and 20.1, respectively. Other parameters are the same as those described in the caption of Fig. 2.

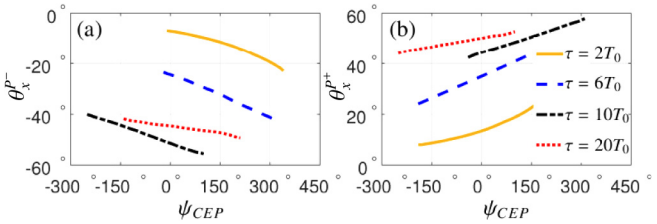

FIG. 10. (a), (b) The variations of $\theta_x^{P^-}$ and $\theta_x^{P^+}$ with respect to the CEP, respectively. The yellow-solid, blue-dashed, and black-dash-dotted curves represent the cases of the focused Gaussian laser pulse with $\tau = 2, 6$, and $10T_0$, respectively, and the red-dotted curves show the case of a flat-top Gaussian laser pulse with $\tau = 20T_0$. Other parameters are the same as those described in the caption of Fig. 2.

laser pulses with $\tau = 2T_0$ (yellow), $6T_0$ (blue), and $10T_0$ (black), respectively. As the laser pulse duration increases, the gradients of the variations of $\theta_x^{P^-}$ and $\theta_x^{P^+}$ decrease slightly. The CEP resolutions for all cases are close to 0.1°. Moreover, the case of a flat-top Gaussian laser pulse with a pulse envelop of $\exp(-t^4/\tau^4)$ and $\tau = 20T_0$ (red) is shown as well. Since this method detects the CEP via the electron reflection at the rising edge of the laser pulse, it works well also for the long flat-top laser pulses. The CEP resolution for the given parameters is $\sim 0.3^\circ$.

The role of the initial kinetic energy ε_i of the electron bunch is investigated as well, see Fig. 11. As ε_i increases from 1 keV to 1 MeV with a constant $\xi = 20$, the CEP resolution reduces from $\sim 0.1^\circ$ to $\sim 0.25^\circ$ slowly, and the optimal ε_i fulfills the condition $\gamma \sim \xi/100$. Note that in the considered scheme of CEP determination, the laser intensity and the electron energy are both limited from above such that the stochasticity effects of radiation are negligible,

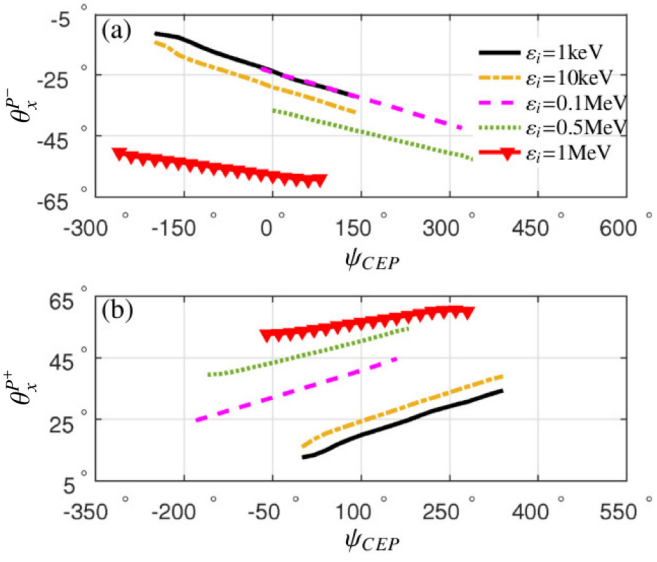

FIG. 11. (a), (b) The variations of $\theta_x^{P^-}$ and $\theta_x^{P^+}$ corresponding to θ_x of P^- and P^+ with respect to $\psi_{\rm CEP}$, respectively. The black-solid, yellow-dash-dotted, magenta-dashed, green-dotted, and red-triangle curves show the cases with $\varepsilon_i = 1$ keV, 10 keV, 0.1 MeV, 0.5 MeV, and 1 MeV, respectively. Other parameters are the same as those described in the caption of Fig. 2.

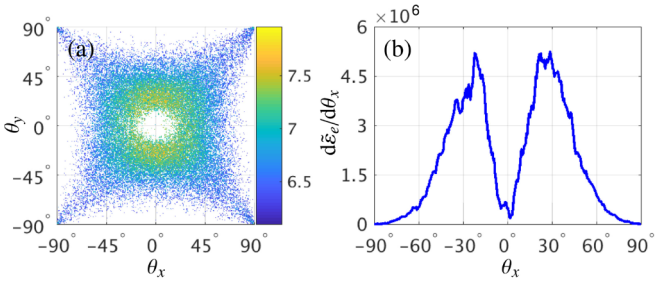

FIG. 12. (a) Angle-resolved electron energy $\log_{10}[d^2\varepsilon_e/(d\theta_x d\theta_y)]$ rad^{-2} vs. θ_x and θ_y and (b) $d\tilde{\varepsilon}_e/d\theta_x$ and vs. θ_x, with $\xi = 600$ and $\varepsilon_i = 150$ MeV. Other parameters are the same as those described in the caption of Fig. 2.

i.e., $\chi \sim 10^{-6}\xi\gamma \ll 1$. Otherwise, the CEP signatures vanish completely; see Fig. 12. We consider $\xi = 600$ and $\varepsilon_i = 150$ MeV ($\chi_{\rm max} \sim 1$). For this case, the stochasticity effects of the radiation significantly modify the electron dynamics, and the impacts of the CEP on the electron dynamics are removed. Consequently, the distribution of electron momenta becomes symmetric with respect to θ_x.

V. CONCLUSION

Concluding, common CEP effects in the nonrelativistic regime of laser-matter interaction are negligible in the case of long laser pulses ($\tau \gtrsim 6T_0$). However, the specific CEP effects in the relativistic regime of interaction, originating from the field asymmetry in the rising edge of the laser pulse, are still significant for multicycle laser pulses. Thus, the dynamics of the relativistic laser-electron beam interaction can be CEP-dependent even in multicycle laser pulses, which, from one side, requires measurement of CEP of the driving laser pulse to control the interaction, and from another side, itself provides a way for the CEP measurement of multicycle pulses. In this paper using this general feature of CEP effects in the relativistic regime, we put forward a simple and realistic method for measuring CEP of multicycle relativistic laser pulses from currently standard ultraintense laser facilities, with an intensity of the order of $I_0 \gtrsim 10^{19}$ W/cm^2, and the laser peak power from tens of terawatt to multi-petawatt region. The method employs the electron-momentum distribution after the interaction. It is shown to be robust with the laser and electron parameters and is applicable for relativistic laser pulses with duration up to 10 cycles (up to 20 cycles for the flat-top laser pulses). The CEP resolution can achieve about 0.1°, one order of magnitude higher than that previously achieved via the x-ray radiation, since the diffraction limitation of an electron is much smaller than that of a photon.

In the near future, with fast development of ultraintense lasers and the broad research interests on strong laser physics, the accurate determination of CEP of relativistic laser pulses are expected to be in great demand.

ACKNOWLEDGMENTS

This work is supported by the Science Challenge Project of China (Grants No. TZ2016005 and No. TZ2016099), the

National Key Research and Development Program of China (Grant No. 2018YFA0404801), the National Natural Science Foundation of China (Grants No. 11874295, No. 11804269, No. 11875219, No. U1532263, No. 11520101003, and No. 11861121001), and the Laser Fusion Research Center Funds for Young Talents (Grant No. RCFPD2-2018-4).

APPENDIX

In the "Landau-Lifshitz" method, the effects of radiation reaction on electron dynamics are included by means of an additional force besides the Lorentz force. The radiation reaction force is written as [57,58]

$$m\frac{du^{\mu}}{d\tilde{\tau}} = eF^{\mu j}u_j + f^{\mu},$$

where

$$f^{\mu} = \frac{2e^3}{3m}(\partial_{\alpha}F^{\mu\nu}u_{\nu}u^{\alpha}) + \frac{2e^4}{3m^2}[F^{\mu\nu}F_{\nu\alpha}u^{\alpha} + (F^{\nu\beta}u_{\beta}F_{\nu\alpha}u^{\alpha})u^{\mu}],$$

where $u^{\alpha} = (\gamma, \gamma\mathbf{v})$ is four-velocity of the electron, $F^{\mu\nu}$ the electromagnetic tensor relative to the total electromagnetic field acting on the electron, and $\tilde{\tau}$ the proper time,

$$\frac{d}{d\tilde{\tau}} = (k\cdot u)\frac{d}{d\tilde{\eta}}.$$

We have performed simulations of the laser-electron interactions with "Landau-Lifshitz" equation and compared them with those of the Monte Carlo method and the Newton equation, as shown in Fig. 13. With the given parameters of $\xi = 20$ and $\varepsilon_i = 0.1$ MeV ($\chi \ll 1$), the three methods give the same results.

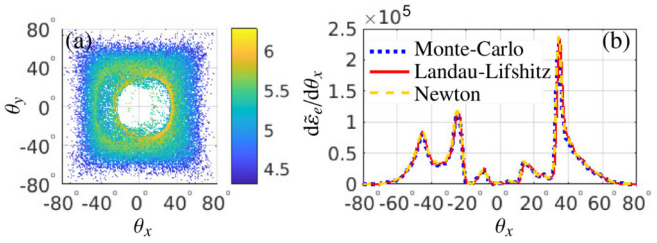

FIG. 13. (a) Angle-resolved electron energy $\log_{10}[d^2\varepsilon_e/(d\theta_x d\theta_y)]$ vs. θ_x and θ_y, simulated by the "Landau-Lifshitz" method. (b) $d\tilde{\varepsilon}_e/d\theta_x$ vs. θ_x with $\psi_{\mathrm{CEP}} = 0^{\circ}$, and the blue-dotted, red-solid, and yellow-dashed curves are calculated by the Monte Carlo method, "Landau-Lifshitz" equation, and Lorentz motion equation, respectively. $\xi = 20$, $\varepsilon_i = 0.1$ MeV, and other parameters are the same as those described in the caption of Fig. 2.

[1] D. Strickland and G. Mourou, Opt. Commun. **55**, 447 (1985).
[2] The Vulcan facility, http://www.clf.stfc.ac.uk/Pages/The-Vulcan-10-Petawatt-Project.aspx.
[3] The Extreme Light Infrastructure (ELI), http://www.eli-beams.eu/en/facility/lasers/.
[4] Exawatt Center for Extreme Light Studies (XCELS), http://www.xcels.iapras.ru/.
[5] V. Yanovsky, V. Chvykov, G. Kalinchenko, P. Rousseau, T. Planchon, T. Matsuoka, A. Maksimchuk, J. Nees, G. Cheriaux, G. Mourou, and K. Krushelnick, Opt. Express **16**, 2109 (2008).
[6] G. A. Mourou, T. Tajima, and S. V. Bulanov, Rev. Mod. Phys. **78**, 309 (2006).
[7] E. Esarey, C. B. Schroeder, and W. P. Leemans, Rev. Mod. Phys. **81**, 1229 (2009).
[8] A. Macchi, M. Borghesi, and M. Passoni, Rev. Mod. Phys. **85**, 751 (2013).
[9] M. M. Murnane, H. C. Kapteyn, M. D. Rosen, and R. W. Falcone, Science **251**, 531 (1991).
[10] S. Corde, K. Ta Phuoc, G. Lambert, R. Fitour, V. Malka, A. Rousse, A. Beck, and E. Lefebvre, Rev. Mod. Phys. **85**, 1 (2013).
[11] H. Schwoerer, S. Pfotenhauer, O. Jäckel, K.-U. Amthor, B. Liesfeld, W. Ziegler, R. Sauerbrey, K. W. D. Ledingham, and T. Esirkepov, Nature **439**, 445 (2006).
[12] T.-P. Yu, A. Pukhov, Z.-M. Sheng, F. Liu, and G. Shvets, Phys. Rev. Lett. **110**, 045001 (2013).
[13] M. Tabak, J. Hammer, M. E. Glinsky, W. L. Kruer, S. C. Wilks, J. Woodworth, E. M. Campbell, M. D. Perry, and R. J. Mason, Phys. Plasmas **1**, 1626 (1994).
[14] J. D. Lindl, P. Amendt, R. L. Berger, S. G. Glendinning, S. H. Glenzer, S. W. Haan, R. L. Kauffman, O. L. Landen, and L. J. Suter, Phys. Plasmas **11**, 339 (2004).
[15] H. S. Park, O. A. Hurricane, D. A. Callahan, D. T. Casey, E. L. Dewald, T. R. Dittrich, T. Döppner, D. E. Hinkel, L. F. Berzak Hopkins, S. Le Pape, T. Ma, P. K. Patel, B. A. Remington, H. F. Robey, J. D. Salmonson, and J. L. Kline, Phys. Rev. Lett. **112**, 055001 (2014).
[16] D. Ryutov, R. P. Drake, J. Kane, E. Liang, B. A. Remington, and W. M. Woodvasey, Astrophys. J. **518**, 821 (1999).
[17] Y.-F. Li, Y.-T. Li, W.-M. Wang, D.-W. Yuan, B.-J. Zhu, J.-Y. Zhong, H.-G. Wei, F. Li, B. Han, K. Zhang, X.-X. Pei, Z. Zhang, J.-R. Zhao, C. Liu, G.-Q. Liao, Z.-H. Fang, C. Wang, X.-G. Wang, Y. Sakawa, Y.-J. Rhee, X. Lu, N. Hua, B.-Q. Zhu, T. Morita, Y. Kuramitsu, X.-G. Huang, S.-Z. Fu, J.-Q. Zhu, G. Zhao, and J. Zhang, Sci. Rep. **8**, 463 (2018).
[18] B. A. Remington, R. P. Drake, and D. D. Ryutov, Rev. Mod. Phys. **78**, 755 (2006).
[19] X. Liu, H. Rottke, E. Eremina, W. Sandner, E. Goulielmakis, K. O. Keeffe, M. Lezius, F. Krausz, F. Lindner, M. G. Schätzel, G. G. Paulus, and H. Walther, Phys. Rev. Lett. **93**, 263001 (2004).
[20] T. Rathje, A. M. Sayler, S. Zeng, P. Wustelt, H. Figger, B. D. Esry, and G. G. Paulus, Phys. Rev. Lett. **111**, 093002 (2013).
[21] T. M. Fortier, P. A. Roos, D. J. Jones, S. T. Cundiff, R. D. R. Bhat, and J. E. Sipe, Phys. Rev. Lett. **92**, 147403 (2004).
[22] G. Sansone, C. Vozzi, S. Stagira, M. Pascolini, L. Poletto, P. Villoresi, G. Tondello, S. De Silvestri, and M. Nisoli, Phys. Rev. Lett. **92**, 113904 (2004).

[23] I. P. Christov, M. M. Murnane, and H. C. Kapteyn, Phys. Rev. Lett. **78**, 1251 (1997).

[24] N. Ishii, K. Kaneshima, K. Kitano, T. Kanai, S. Watanabe, and J. Itatani, Nat. Commun. **5**, 3331 (2014).

[25] M. Boca and V. Florescu, Phys. Rev. A **80**, 053403 (2009).

[26] F. Mackenroth, A. Di Piazza, and C. H. Keitel, Phys. Rev. Lett. **105**, 063903 (2010).

[27] D. Seipt and B. Kämpfer, Phys. Rev. A **88**, 012127 (2013).

[28] F. Hebenstreit, R. Alkofer, G. V. Dunne, and H. Gies, Phys. Rev. Lett. **102**, 150404 (2009).

[29] K. Krajewska and J. Z. Kamiński, Phys. Rev. A **86**, 052104 (2012).

[30] N. Abdukerim, Z.-L. Li, and B.-S. Xie, Phys. Lett. B **726**, 820 (2013).

[31] S. Meuren, C. H. Keitel, and A. Di Piazza, Phys. Rev. D **93**, 085028 (2016).

[32] A. I. Titov, B. Kämpfer, A. Hosaka, T. Nousch, and D. Seipt, Phys. Rev. D **93**, 045010 (2016).

[33] M. J. A. Jansen and C. Müller, Phys. Rev. D **93**, 053011 (2016).

[34] J. X. Li, Y. Y. Chen, K. Z. Hatsagortsyan, and C. H. Keitel, Phys. Rev. Lett. **120**, 124803 (2018).

[35] T. Tajima and J. M. Dawson, Phys. Rev. Lett. **43**, 267 (1979).

[36] S. P. D. Mangles, C. D. Murphy, Z. Najmudin, A. G. R. Thomas, J. L. Collier, A. E. Dangor, E. J. Divall, P. S. Foster, J. G. Gallacher, C. J. Hooker, D. A. Jaroszynski, A. J. Langley, W. B. Mori, P. A. Norreys, F. S. Tsung, R. Viskup, B. R. Walton, and K. Krushelnick, Nature **431**, 535 (2004).

[37] J. Faure, Y. Glinec, A. Pukhov, S. Kiselev, S. Gordienko, E. Lefebvre, J.-P. Rousseau, F. Burgy, and V. Malka, Nature **431**, 541 (2004).

[38] W. P. Leemans, B. Nagler, A. J. Gonsalves, C. Tóth, K. Nakamura, C. G. R. Geddes, E. Esarey, C. B. Schroeder, and S. M. Hooker, Nat. Phys. **2**, 696 (2006).

[39] B. M. Hegelich, B. J. Albright, J. Cobble, K. Flippo, S. Letzring, M. Paffett, H. Ruhl, J. Schreiber, R. K. Schulze, and J. C. Fernández, Nature **439**, 441 (2006).

[40] G. G. Paulus, F. Grasbon, H. Walther, P. Villoresi, M. Nisoli, S. Stagira, E. Priori, and S. De Silvestri, Nature **414**, 182 (2001).

[41] R. Holzwarth, T. Udem, T. W. Hänsch, J. C. Knight, W. J. Wadsworth, and P. S. J. Russell, Phys. Rev. Lett. **85**, 2264 (2000).

[42] P. Dombi, A. Apolonski, C. Lemell, G. G. Paulus, M. Kakehata, R. Holzwarth, T. Udem, K. Torizuka, J. Burgdörfer, T. W. Hänsch, and F. Krausz, New J. Phys. **6**, 39 (2004).

[43] E. Goulielmakis, M. Uiberacker, R. Kienberger, A. Baltuska, V. Yakovlev, A. Scrinzi, T. Westerwalbesloh, U. Kleineberg, U. Heinzmann, M. Drescher, and F. Krausz, Science **305**, 1267 (2004).

[44] A. Di Piazza, C. Müller, K. Z. Hatsagortsyan, and C. H. Keitel, Rev. Mod. Phys. **84**, 1177 (2012).

[45] J. Wang, J. Feng, C. Zhu, Y. Li, Y. He, D. Li, J. Tan, J. Ma, and L. Chen, Plasma Phys. Controlled Fusion **60**, 034004 (2018).

[46] J. Maxson, D. Cesar, G. Calmasini, A. Ody, P. Musumeci, and D. Alesini, Phys. Rev. Lett. **118**, 154802 (2017).

[47] Y. Qi, M. Pei, D. Qi, Y. Yang, T. Jia, S. Zhang, and Z. Sun, J. Phys. Chem. Lett. **6**, 3867 (2015).

[48] P. Zhu, Y. Zhu, Y. Hidaka, L. Wu, J. Cao, H. Berger, J. Geck, R. Kraus, S. Pjerov, Y. Shen, R. I. Tobey, J. P. Hill, and X. J. Wang, New J. Phys. **17**, 063004 (2015).

[49] C. S. Shen and D. White, Phys. Rev. Lett. **28**, 455 (1972).

[50] R. Duclous, J. G. Kirk, and A. R. Bell, Plasma Phys. Controlled Fusion **53**, 015009 (2011).

[51] N. Neitz and A. Di Piazza, Phys. Rev. Lett. **111**, 054802 (2013).

[52] H. R. Reiss, J. Math. Phys. (NY) **3**, 59 (1962).

[53] V. I. Ritus, J. Sov. Laser Res. **6**, 497 (1985).

[54] N. V. Elkina, A. M. Fedotov, I. Y. Kostyukov, M. V. Legkov, N. B. Narozhny, E. N. Nerush, and H. Ruhl, Phys. Rev. ST Accel. Beams **14**, 054401 (2011).

[55] C. P. Ridgers, J. G. Kirk, R. Duclous, T. G. Blackburn, C. S. Brady, K. Bennett, T. D. Arber, and A. R. Bell, J. Comput. Phys. **260**, 273 (2014).

[56] D. Green and C. Harvey, Comput. Phys. Commun. **192**, 313 (2015).

[57] L. D. Landau and E. M. Lifshitz, *The Classical Theory of Fields*, 2nd ed. (Elsevier, Oxford, 1975), Chap. 76.

[58] A. Zhidkov, J. Koga, A. Sasaki, and M. Uesaka, Phys. Rev. Lett. **88**, 185002 (2002).

[59] Y. I. Salamin and C. H. Keitel, Phys. Rev. Lett. **88**, 095005 (2002).

[60] Y. I. Salamin, G. R. Mocken, and C. H. Keitel, Phys. Rev. ST Accel. Beams **5**, 101301 (2002).

[61] X. Wang, R. Zgadzaj, N. Fazel, Z. Li, S. A. Yi, X. Zhang, W. Henderson, Y.-Y. Chang, R. Korzekwa, H.-E. Tsai, C.-H. Pai, H. Quevedo, G. Dyer, E. Gaul, M. Martinez, A. C. Bernstein, T. Borger, M. Spinks, M. Donovan, V. Khudik, G. Shvets, T. Ditmire, and M. C. Downer, Nat. Commun. **4**, 1988 (2013).

[62] W. P. Leemans, A. J. Gonsalves, H.-S. Mao, K. Nakamura, C. Benedetti, C. B. Schroeder, C. Tóth, J. Daniels, D. E. Mittelberger, S. S. Bulanov, J.-L. Vay, C. G. R. Geddes, and E. Esarey, Phys. Rev. Lett. **113**, 245002 (2014).

[63] B. Wolter, M. G. Pullen, A. T. Le, M. Baudisch, K. Doblhoff-Dier, A. Senftleben, M. Hemmer, C. D. Schroter, J. Ullrich, T. Pfeifer, R. Moshammer, S. Grafe, O. Vendrell, C. D. Lin, and J. Biegert, Science **354**, 308 (2016).

[64] R. P. Chatelain, V. R. Morrison, B. L. M. Klarenaar, and B. J. Siwick, Phys. Rev. Lett. **113**, 235502 (2014).

[65] J. H. Sung, H. W. Lee, J. Y. Yoo, J. W. Yoon, C. W. Lee, J. M. Yang, Y. J. Son, Y. H. Jang, S. K. Lee, and C. H. Nam, Opt. Lett. **42**, 2058 (2017).

[66] D. Adolph, M. Möller, J. Bierbach, M. Schwab, A. Sävert, M. Yeung, A. M. Sayler, M. Zepf, M. C. Kaluza, and G. G. Paulus, Appl. Phys. Lett. **110**, 081105 (2017).